



Enhancing electroreduction activity and selectivity of N₂-to-NH₃ through proton-feeding adjustments in Ag@AgP₂@Ni-CoP@C core-shell nanowires

Shoushuang Huang ^{a,1}, Jinmei Bao ^{a,1}, Deyu Xiang ^a, Chunyan Gao ^a, Kaimei Peng ^{b,*}, Qiaochuan Chen ^{c,*}, Shuzhen Ma ^a, Yong Jiang ^{a,*²}, Zhangjun Hu ^{d,*²}, Jiujun Zhang ^e

^a School of Environmental and Chemical Engineering, Shanghai University, Shanghai 200444, China

^b School of Chemistry and Chemical Engineering, Qiannan Normal University for Nationalities, Duyun 558000, China

^c School of Computer Engineering and Science Shanghai University, 99 Shangda Road, Shanghai 200444, China

^d Division of Molecular Surface Physics & Nanoscience, Department of Physics, Chemistry and Biology, Linköping University, Linköping 58183, Sweden

^e Institute for Sustainable Energy/College of Sciences, Shanghai University, Shanghai 200444, China



ARTICLE INFO

Keywords:

CoP
Nitrogen reduction reaction
Heterostructure
Nanowire
Electrocatalysis

ABSTRACT

The synthesis of NH₃ via electrochemical N₂ fixation at ambient conditions has been proposed as a promising alternative to the traditional Haber-Bosch process. However, the development of highly efficient and selective electrocatalysts remains a challenge. In this study, uniform Ag@AgP₂@Ni-CoP@C core-shell nanowires were synthesized using a template-engaged strategy. The merging of conductive Ag core with active AgP₂ and porous carbon-coated Ni-doped CoP shells favors the mass and electron transfers, effectively lowering the activation energy toward the reduction of N₂ to NH₃. Density functional theory (DFT) calculations further indicates that the sandwiched AgP₂ layer plays crucial roles in promoting electrocatalytic kinetics and suppressing the competitive hydrogen evolution reactions. Benefiting from these advantages, the titled catalyst achieved a high NH₃ yield of 16.84 μg h⁻¹ mg_{cat}⁻¹ at -0.4 V (vs. reversible hydrogen electrode, RHE) and a high Faradaic efficiency of 21.7 % at -0.3 V vs. RHE, as well as high electrochemical and structure stability.

1. Introduction

In recent years, the electrocatalytic reduction of nitrogen (N₂) to ammonia (NH₃) at room temperature and atmospheric pressure, also referred to as the nitrogen reduction reaction (NRR), has received significant attention as a potential alternative to the Haber-Bosch process for the synthesis of NH₃ [1–3]. This NRR reaction can be represented as N₂ + 6 H⁺ + 6e⁻ → 2NH₃. Despite the potential benefits of this approach, low yields of NH₃ and Faraday efficiency (FE) have prevented its widespread adoption due to the difficulties in adsorbing N₂, challenging cleavage of N≡N triple bonds and competing hydrogen evolution reactions (HER) [4–7]. Therefore, the development of more efficient and stable catalysts for electrochemical ammonia synthesis is significantly important.

Up to now, a wide range of transition metal-based catalysts, including phosphides [8,9], sulfides [10], oxides [11] and nitride [12, 13], have become extensively investigated and have achieved great

success in electrocatalytic reduction of N₂ to NH₃. Among these, cobalt phosphide (CoP)-based compounds have been considered as desirable NRR electrocatalysts due to their abundant reserves, rich redox chemistry and unoccupied d orbital of Co, which can facilitate the adsorption and activation of N₂ by accepting and donating electrons. Recent studies have demonstrated the effectiveness of CoP-based compounds as NRR electrocatalysts [14–17]. For example, Xu et al. [16] found that CoP hollow nanocages could effectively catalyze the reduction of N₂, with a NH₃ yield of 10.78 μg h⁻¹ mg_{cat}⁻¹ at -0.4 V vs. RHE and a FE of 7.36 % at 0 V vs. RHE. Meng et al. [15] reported that the oxidized CoP particles encapsulated in carbon nanotubes could offer a high NH₃ yield of 39.58 μg h⁻¹ mg_{cat}⁻¹ and a FE of 19.4 % at -0.5 V vs. RHE, further highlighting the potential of CoP-based compounds as NRR electrocatalysts.

In recent years, significant efforts aimed at exploring phosphides for NRR, however, achieving high yields of NH₃ and FE remains a challenge, primarily due to three factors [18–20]: (1) the unsatisfactory intrinsic activity of phosphides; (2) the competitive HER lead to the preferential

* Corresponding authors.

E-mail addresses: pkmchem@sgmtu.edu.cn (K. Peng), qcchen@shu.edu.cn (Q. Chen), jiangyong@shu.edu.cn (Y. Jiang), zhangjun.hu@liu.se (Z. Hu).

¹ S. Huang and J. Bao contributed equally to the work

² Further information and requests for resources should be directed to and will be fulfilled by the lead contacts.

adsorption of H atoms over N atoms; (3) the strong tendency of nanostructured phosphides to agglomerate, reducing the exposure of active sites and preventing the adsorption of N_2 on the catalyst surface. To address these challenges, one effective strategy is the establishment of heterojunctions through hybridization of suitable components. The crucial role of interfaces in heterostructured electrocatalysts involves not only increasing the exposure of highly active sites but also the redistribution of electrons around active centers [21]. In this regards, integrating the merits and the overcoming of the weaknesses of individual components can effectively enhance charge transportation and tailor the chemisorption free energies of the NRR intermediates, leading to improved NH_3 yield and FF compared to single-component counterparts [22–25]. Therefore, the construction of elaborately designed CoP-based heterostructured catalysts is a promising and reliable approach to achieve highly efficient NRR performance with excellent selectivity. Despite the recent progress in the development of efficient electrocatalysts constructed using an interface engineering strategy for NRR, many of these heterointerface electrocatalysts tend to simultaneously enhance the activity of HER due to the strong competition between NRR and HER. Therefore, it is crucial to develop electrocatalysts for NRR that can selectively adsorb N_2 over H atoms through interface engineering.

Herein, uniform Ag@AgP₂@Ni-CoP@C core-shell nanowires were synthesized via a template-engaged strategy. The process began with preparing uniform Ag nanowires as structural templates, followed by coating with a dense ZIF-67 layer, an adjustable ions-exchange/chemical etching process, and phosphating treatment. The merging of conductive Ag core with active AgP₂ and porous carbon-coated Ni-doped CoP (Ni-CoP) shell resulted in robust multiple core-shell structure that favored the mass transfer from the electrolyte to the electrodes and the electron transfer to the active sites, then effectively help to anchor and activate the N_2 molecules and lower the activation energy toward the reduction of N_2 to NH_3 . Benefiting from these advantages, the resulting Ag@AgP₂@Ni-CoP@C catalyst showed excellent NRR performance, including high Faradaic efficiency, long-term durability, and a maximum NH_3 yield of 16.84 $\mu g\ h^{-1}\ mg_{cat}^{-1}$ at -0.4 V vs. RHE. The Faradaic efficiency was also highest at -0.3 V vs. RHE, reaching a value of 21.7 %. This work may offer a promising approach for the preparation of multiple core-shell nanowires that can be used in the energy storage and conversion system.

2. Experimental section

2.1. Synthesis of Ag@ZIF-67 core-shell nanowires

The synthesis of Ag@ZIF-67 core-shell nanowires was performed using an in-situ growth process, in which a layer of ZIF-67 was grown on Ag nanowires. The Ag nanowires were synthesized using the method described by Chen [26]. To prepare the Ag@ZIF-67 core-shell nanowires, a solution referred to as Solution A was prepared by stirring a mixture of 50 mg of freshly synthesized Ag nanowires, 0.3 g of poly-vinylpyrrolidone, and 12.5 mL of methanol for 10 min. Separately, Solutions B and C were prepared by dissolving 100 mg of $Co(NO_3)_2 \cdot 6 H_2O$ and 1.48 g of 2-methylimidazole (2-MeIM) in 12.5 mL and 25.0 mL of methanol, respectively. These solutions were then added into Solution A and the mixed solution was stirred for an additional 2 h. After that, the resulting product, named as Ag@ZIF-67, was collected via centrifugation, washed three times with methanol, and finally dried in an oven at 60 °C for 12 h.

2.2. Synthesis of Ag@Ni-ZIF-67

The preparation of Ag@Ni-ZIF-67 was accomplished through a simple ion-exchange process. To begin, 20 mg of Ag@ZIF-67 powder was dispersed in 20 mL of ethanol and stirred for 10 mins. Subsequently, 20 mg of $Ni(NO_3)_2 \cdot 6 H_2O$ was added to the solution, which was then

stirred for an additional hour. The resulting precipitate was collected via centrifugation and washed repeatedly with methanol.

2.3. Synthesis of Ag@AgP₂@Ni-CoP@C

The Ag@AgP₂@Ni-CoP@C heterostructured nanowires were prepared using a high-temperature phosphatization process. Specifically, a porcelain boat containing 10 mg of Ag@Ni-ZIF-67 and 100 mg of $Na_2PO_2 \cdot H_2O$ was covered with a glass sheet and placed inside a quartz tube. The tube was heated to 350 °C at a rate of 2 °C/min and maintained at this temperature for 120 min. After cooling to room temperature, a black powder denoted as Ag@AgP₂@Ni-CoP@C was obtained. For comparison, CoP and Ag@AgP₂ nanowires were also synthesized employing a similar phosphatization process utilizing ZIF-67 and Ag nanowires as the initial materials. For the Ni-doped CoP, an ion-exchange reaction was initially carried out between ZIF-67 and $Ni(NO_3)_2$, followed by a similar phosphorization treatment.

2.4. Characterizations

The morphology and microstructure of the samples were characterized using field emission scanning electron microscopy (JSM-7500 F), transmission electron microscopy (JEM-200CX), and high-resolution transmission electron microscopy (HRTEM, JSM-2010 F). The element mapping and linear composition scans were performed using energy-dispersive X-ray spectroscopy (EDS) in conjunction with TEM. The crystal structure and phase of the products were determined using X-ray diffraction (D/Max-2500 XRD) in the range of 5–80° with a scan speed of 8°/min. The composition and valence states of the catalysts were analyzed using X-ray photoelectron spectroscopy (Thermo Escalab 250XI XPS). ICP analysis was conducted using an Agilent 5110 instrument for measurement. The surface area and porosity analyzer (Quantachrome, USA Qudrasorb SI) was employed to evaluate the pore volume, pore size, and surface area of the samples using the Brunauer-Emmett-Teller (BET) method for surface area determination and pore-size distribution curves.

2.5. Electrochemical measurements

The nitrogen reduction reaction was evaluated using an H-type cell with a Nafion 117 membrane separating the two chambers, each of which contained 30 mL of 0.1 M Na_2SO_4 electrolyte. Electrochemical measurements were performed using a CHI660e workstation with a three-electrode system. A carbon paper loaded with catalyst served as the working electrode, Ag/AgCl as the reference electrode, and a graphite rod as the counter electrode. The working electrode was prepared by mixing 2.5 mg of catalyst with 120 μL of ethanol, 120 μL of water, and 10 μL of Nafion solution, and ultrasonication the mixture for at least 0.5 h to obtain a homogenous “ink”. This “ink” was then applied to a $0.5 \times 0.5\ cm^2$ piece of carbon paper, 20 μL at a time, and dried in a vacuum oven.

2.6. Calculation of NH_3 yield and FE

The concentration of NH_3 in Na_2SO_4 electrolyte was determined using the indolophenol blue method [27]. To do this, 2 mL of electrolytic solution was taken from the cathode chamber and mixed with 2 mL of 1 M NaOH solution (containing 5 wt% $C_6H_5Na_3O_7$ and 5 wt% $C_7H_6O_3$), 1 mL of 0.05 M NaClO, and 0.2 mL of 1 wt% $C_5FeN_6Na_2O \cdot 2 H_2O$. After the resulting solution was kept in the dark at ambient conditions for 2 h, UV-Vis absorption spectra were measured at 655 nm. The production of N_2H_4 was quantified using the approach of Watt and Chrissip [28]. This involved mixing 5.99 g of $C_6H_{11}NO$, 30 mL of HCl, and 300 mL of ethanol to create a chromogenic solution. Then, 5 mL of electrolytic solution was taken from the cathode chamber, mixed with 5 mL of the chromogenic solution, and allowed to stand for 10 mins. The absorption

spectra were measured using a UV-Vis spectrophotometer, and the amount of hydrazine formed during electrolysis was calculated based on a concentration-absorbance curve at 455 nm. The ammonia yield was calculated using the formula: $\gamma_{\text{NH}_3} = (c_{\text{NH}_3} \times V)/(t \times m_{\text{cat}})$, where c represents the total mass concentration of NH_3 , V represents the volume of the electrolyte, t represents the duration of the electrolysis reaction, and m represents the loading mass of the catalyst. The Faraday efficiency of the electrolysis process was calculated using the formula: $\text{FE} = 3 F \times n_{\text{NH}_3}/Q$, where F represents the Faraday constant, Q represents the charge, and n represents the total molar mass of NH_3 .

2.7. Density functional theory (DFT) calculations

DFT calculations were performed using the Vienna ab Initio simulation package (VASP) with projector augmented wave (PAW) potentials and the generalized gradient approximation (GGA) Perdew-Burke-Ernzerhof (PBE) functional for electron-ion interaction and exchange-correlation energy, respectively. The plane wave basis cut off energy was set to 400 eV, and the convergence criteria for total energy and force were set to 10^{-5} eV and $0.02 \text{ eV } \text{\AA}^{-1}$, respectively. Based on the structural characterization, an interface model of the $\text{AgP}_2 @\text{Ni-CoP}$ heterostructure was constructed. The model consisted of the (111) plane of CoP and the (024) plane of AgP_2 , with a lattice mismatch of 3.37 %. Additionally, a Ni-doped CoP model was created by substituting one Ni atom for Co atom on the surface of CoP. A vacuum distance of 15 Å was imposed in the z direction to eliminate interactions between periodic images. The adsorption energy (E_{ads}) of the N_2 molecule and Gibbs free energy of adsorption hydrogen (ΔG_{H^*}) was calculated according to the computational hydrogen electrode approach [29,30].

3. Results and discussion

Fig. 1 depicts the schematic process for the synthesis of $\text{Ag}@\text{AgP}_2@\text{Ni-CoP}@C$ heterostructured nanowires. The synthesis procedure initiated with the dispersion of AgNO_3 as a precursor and polyvinylpyrrolidone as a surfactant in ethylene glycol. The resulting mixture underwent hydrothermal synthesis at a temperature of 160 °C for a

duration of 6 h. During this process, Ag^+ ions were reduced, leading to the formation of Ag nanowires through a seed-induced growth mechanism with Fe^{3+} as a catalyst. Then, these Ag nanowires were immersed in a methanol solution containing a specified amount of $\text{Co}(\text{NO}_3)_2 \cdot 6 \text{ H}_2\text{O}$ and 2-MeIM. As a result of the coordination reaction between Co^{2+} and 2-MeIM ligands, a solid and dense ZIF-67 layer was deposited on the surface of each Ag nanowire, yielding well-defined $\text{Ag}@\text{ZIF-67}$ core-shell nanowires. Subsequently, a simple ion-exchange/chemical etching strategy was employed to introduce Ni into ZIF-67. In particular, the addition of a small amount of $\text{Ni}(\text{NO}_3)_2 \cdot 6 \text{ H}_2\text{O}$ facilitated the coordination of Ni^{2+} ions with the 2-MeIM ligands, leading to the detachment of Co^{2+} ions from the ZIF-67 framework [31]. This substitution process resulted in the formation of a Ni-ZIF-67 structure, where Ni^{2+} ions replaced Co^{2+} ions within the framework. Finally, the resulting $\text{Ag}@\text{Ni-ZIF-67}$ nanowires were subjected to a controlled phosphating treatment. The shell of Ni-ZIF-67 was

transformed into carbon-coated Ni-doped CoP nanoparticles, while the surface of the Ag nanowires was concurrently converted to crystalline AgP_2 due to its high surface energy and reactive nature. In this way, the novel $\text{Ag}@\text{AgP}_2@\text{Ni-CoP}@C$ multiple core-shell nanowires were obtained.

The morphologies and microstructure of the as-obtained samples, including Ag, $\text{Ag}@\text{ZIF-67}$ and $\text{Ag}@\text{Ni-ZIF-67}$ nanowires, were investigated by scanning electron microscopy (SEM) and transmission electron microscopy (TEM). The SEM images of the as-fabricated Ag nanowires were shown in **Fig. 2a** and **2b**. It can be seen that the diameter of the Ag nanowire ranged from 120 to 180 nm, with a length of 8–10 μm (**Fig. 2c**). The Ag nanowires were employed as the templates for the growth of ZIF-67 layer. It was found that precise control over the amounts of $\text{Co}(\text{NO}_3)_2 \cdot 6 \text{ H}_2\text{O}$ and 2-MeIM is of utmost importance for achieving the desired core-shell structure with high uniformity. Specifically, the optimal amounts of 100 mg of $\text{Co}(\text{NO}_3)_2 \cdot 6 \text{ H}_2\text{O}$ and 1.48 g of 2-MeIM were found to result in uniform and well-defined $\text{Ag}@\text{ZIF-67}$ core-shell nanowires. The SEM image in **Fig. 2d** shows the typical morphology of the as-obtained $\text{Ag}@\text{ZIF-67}$ nanowires. The diameters of the resulting $\text{Ag}@\text{ZIF-67}$ are much larger than the pristine Ag nanowires. Additionally, the broken section (marked with green rectangle) indicates that the Ag nanowires were coated by a dense ZIF-67 shell. This result was also confirmed by the TEM image in **Fig. 2e** and **Fig. S1**, which show that almost all the Ag nanowires were covered by a dense and highly self-assembled ZIF-67 layer. From the magnified TEM image in **Fig. 2f**, we can see that the surfaces of the $\text{Ag}@\text{ZIF-67}$ samples are roughly smooth and dense, and that the thickness of the ZIF-67 shell is about 216 nm. In contrast, using a smaller amount of $\text{Co}(\text{NO}_3)_2 \cdot 6 \text{ H}_2\text{O}$ (33 mg) and 2-MeIM (0.49 g) results in incomplete encapsulation of the Ag nanowires by ZIF-67 (**Fig. S2**), while an excess amount of $\text{Co}(\text{NO}_3)_2 \cdot 6 \text{ H}_2\text{O}$ (300 mg) and 2-MeIM (4.44 g) leads to spontaneous nucleation of ZIF-67, forming numerous individually ZIF-67 nanoparticles (**Fig. S3**). The size and shape of the Ag templates also influence the morphology and size of the resulting $\text{Ag}@\text{ZIF-67}$ core-shell structure (**Fig. S4**). X-ray diffraction (XRD) patterns were collected to investigate the specific phases and crystallinity of the above samples. As shown in **Fig. 2j**, the diffraction peaks of ZIF-67 are good in agreement with the literatures [32,33]. No other miscellaneous peaks appeared, suggesting the high purity of the ZIF-67 precursor. For the $\text{Ag}@\text{ZIF-67}$ sample, the diffraction peaks of ZIF-67 still can be observed. Furthermore, several strong diffraction peaks appeared at 2 Theta of 38.1°, 44.2°, 64.5°, and 77.4°, which can be assigned to the characteristic (111), (200), (220), and (311) crystal planes of Ag (JCPDS No. 04–0783), respectively.

The $\text{Ag}@\text{ZIF-67}$ precursor was employed to synthesize $\text{Ag}@\text{Ni-ZIF-67}$ through a straightforward ion-exchange/chemical etching reaction between $\text{Ag}@\text{ZIF-67}$ and $\text{Ni}(\text{NO}_3)_2 \cdot 6 \text{ H}_2\text{O}$. In order to investigate the effects of varying amounts of $\text{Ni}(\text{NO}_3)_2 \cdot 6 \text{ H}_2\text{O}$ on the morphology and composition of ZIF-67-based intermediates, different quantities of 6.67, 20, and 100 mg of $\text{Ni}(\text{NO}_3)_2 \cdot 6 \text{ H}_2\text{O}$ were utilized. Specifically, when 20 mg of $\text{Ni}(\text{NO}_3)_2 \cdot 6 \text{ H}_2\text{O}$ was used, the surface exhibited a relatively loose and rough appearance compared to the sample with 6.67 mg of $\text{Ni}(\text{NO}_3)_2 \cdot 6 \text{ H}_2\text{O}$ (**Fig. 2g-h** and **Fig. S5**). Detailed TEM images in **Fig. 2i** and **Fig. S6** revealed the presence of numerous open spaces within the shell. Upon annealing, these voids were preserved, leading to the formation of

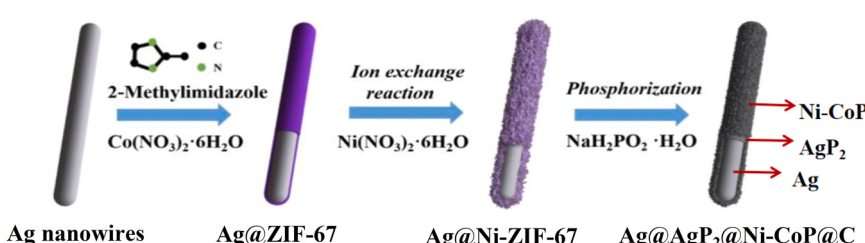


Fig. 1. Schematic representation of the synthesis of $\text{Ag}@\text{AgP}_2 @\text{Ni-CoP}@C$ core-shell nanowires.

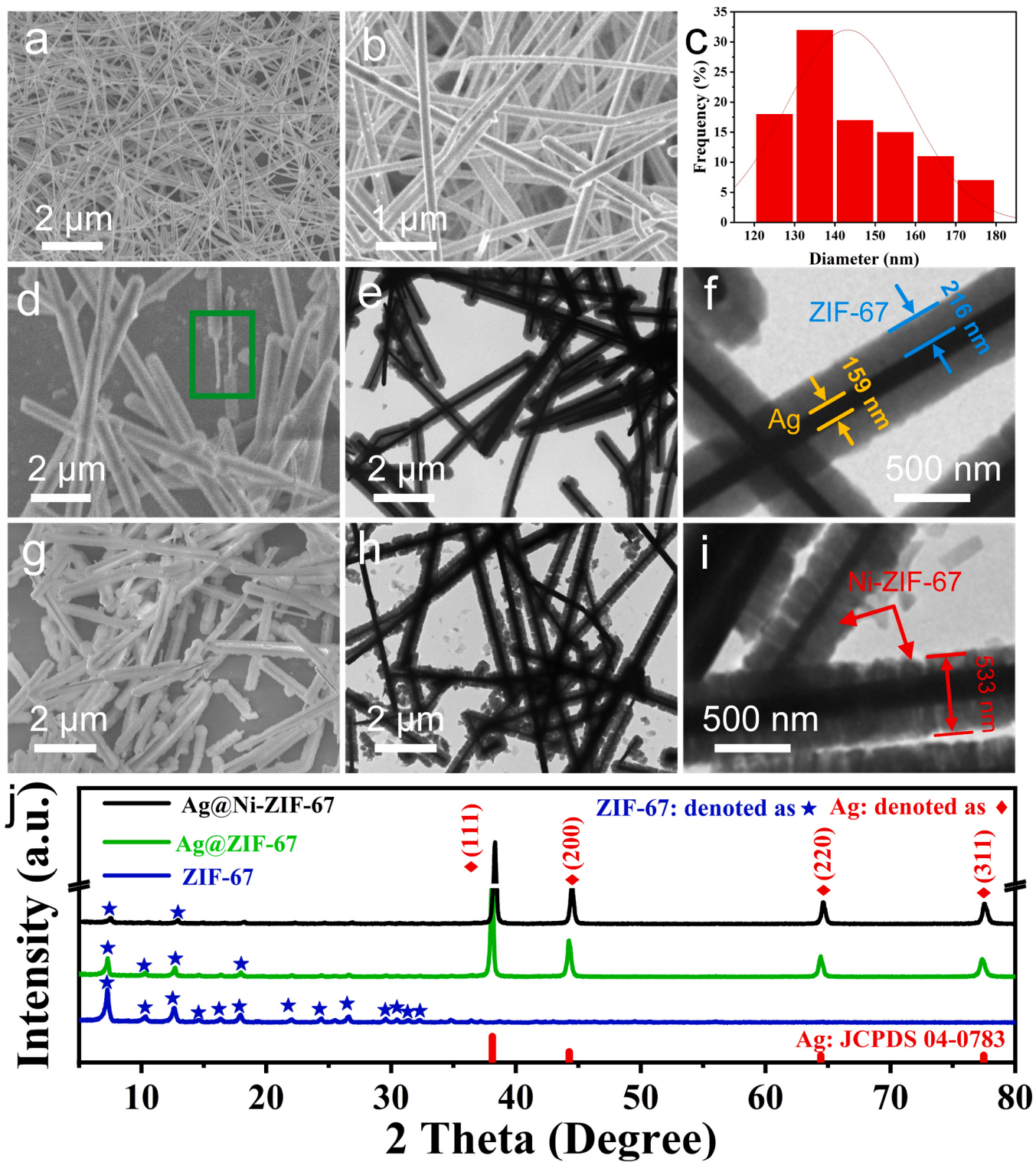


Fig. 2. SEM images (a-b) and diameter distributions (c) of the as-prepared Ag nanowires. SEM (d, g) and TEM (e, f, h, i) images of the Ag@ZIF-67 (d-f) and Ag@Ni-ZIF-67 (g-i) samples. XRD patterns (j) of pure ZIF-67, Ag@ZIF-67 and Ag@Ni-ZIF-67 samples.

the final product, Ag@AgP₂@Ni-CoP@C, possessing a higher number of porous structures. Conversely, when the amount of Ni(NO₃)₂·6 H₂O was increased to 100 mg, the outer layer underwent a transformation into a loosely assembled structure composed of nanosheets (Fig. S7). This transformation can be attributed to the hydrolysis of a significant amount of Ni²⁺, resulting in the generation of a large number of protons. These protons can disrupt the coordinate bond between Co²⁺ ions and 2-

MeIm within the ZIF-67 structure, thereby leading to the etching of ZIF-67 and the release of Co²⁺ ions into the solution, ultimately forming NiCo-LDH [34]. XRD analysis confirmed these observations, demonstrating a gradual decrease in the intensity of ZIF-67 diffraction peaks with increasing amounts of Ni(NO₃)₂·6 H₂O, with complete disappearance observed when 100 mg of Ni(NO₃)₂·6 H₂O was utilized (Fig. S8). These results highlight the significance of precise control over the

amount of $\text{Ni}(\text{NO}_3)_2 \cdot 6 \text{ H}_2\text{O}$ in tuning the Ni to Co ratio within the ZIF-67-based intermediates, which is crucial for tailoring and optimizing the NRR performance of the final catalyst, $\text{Ag}@\text{AgP}_2 @\text{Ni-CoP}@C$.

The $\text{Ag}@\text{Ni-ZIF-67}$ intermediate was converted to $\text{Ag}@\text{AgP}_2 @\text{Ni-CoP}@C$ using $\text{NaH}_2\text{PO}_2 \cdot \text{H}_2\text{O}$ as a phosphorus source at 350°C under the protection of N_2 . As seen in the SEM (Fig. 3a and 3b) and TEM (Fig. 3c) images, the resulting $\text{Ag}@\text{AgP}_2 @\text{Ni-CoP}@C$ sample retained its nanowire shape, but the surface became rather rough. The magnified TEM images in Fig. 3d revealed that the nanowires consisted of an $\text{Ag}@\text{AgP}_2$ core and a layer of Ni-doped CoP as the shell. Additionally, the close observation illustrated that the shell of Ni-doped CoP was composed of numerous nanoparticles (Fig. 3e). Based on the Brunauer–Emmett–Teller (BET) method, the $\text{Ag}@\text{AgP}_2 @\text{Ni-CoP}@C$ nanowires possessed a surface area of $8.17 \text{ m}^2 \text{ g}^{-1}$ with a narrow pore size distribution centred

at 2.8 nm, exhibiting an obvious mesoporous structure (Fig. S9). It's clear that the presence of mesopores structure in the shell can increase electrolyte penetration and diffusion, as well as the utilization of catalytic active sites. Additionally, the core diameter of the nanowires was observed to be thickened. This was due to the chemical reactions between Ag nanowires and PH_3 gas released by NaH_2PO_2 during phosphorization, which made the surface of Ag nanowires in-situ convert to AgP_2 . To provide evidence for the formation of AgP_2 during the phosphorization process, we prepared a new set of samples by directly subjecting the Ag nanowires to phosphorization treatment and performed XRD, SEM, TEM, HRTEM

and element mapping analyses. Although only four strong diffraction peaks belonging to Ag were observed in the XRD pattern (Fig. S10), the average diameter of the resultant product increased by about 30 nm

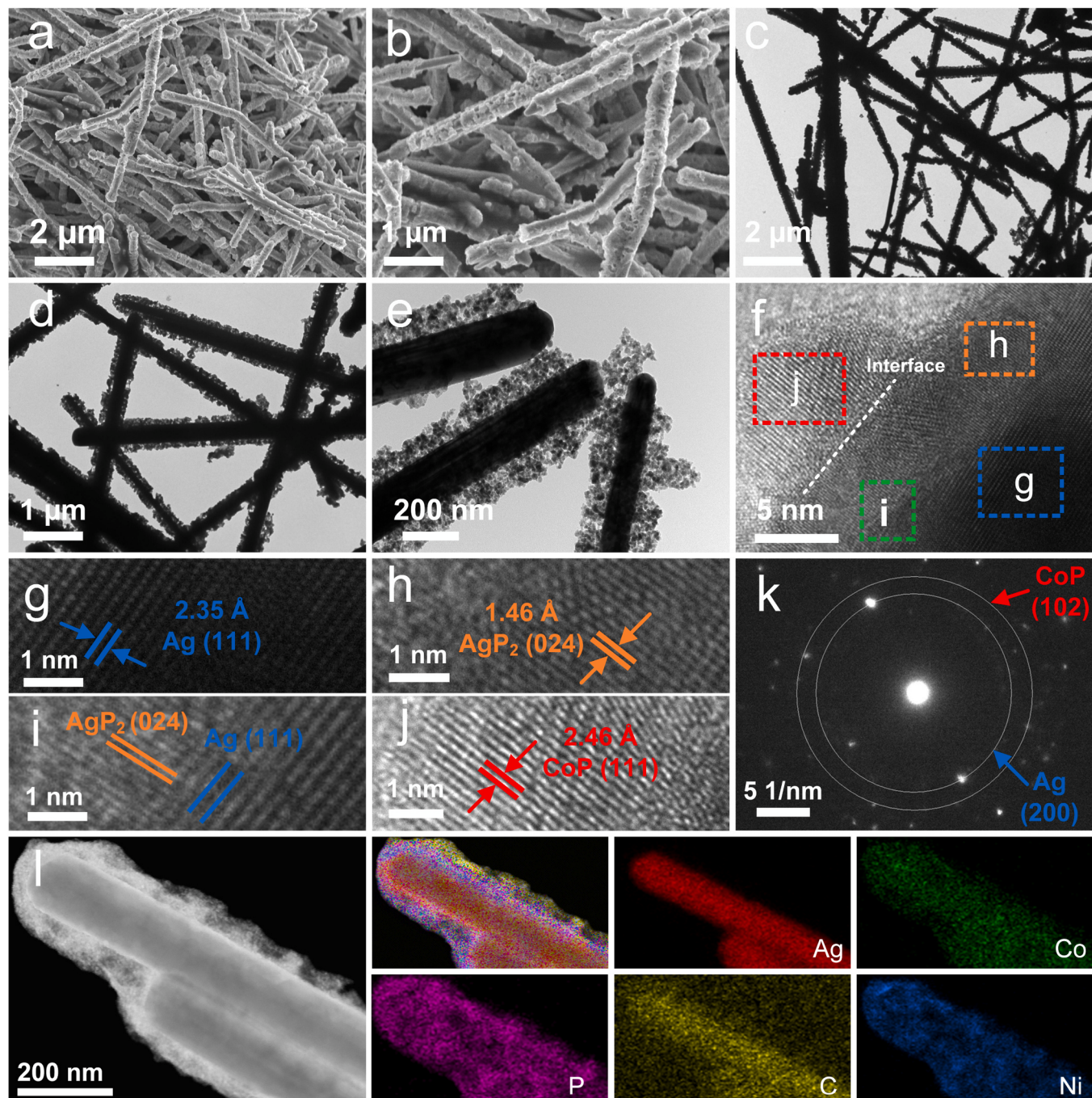


Fig. 3. SEM (a-b), TEM images (c-e), HRTEM (f-j) images, SAED pattern (k) and element mapping (l) of the $\text{Ag}@\text{AgP}_2 @\text{Ni-CoP}@C$ nanowires.

over the pristine Ag nanowires (Fig. S11). Additionally, clear lattice fringes were observed on the surface region of the Ag nanowires, and the interplanar spacings of 0.146 nm well corresponded to the (024) planes of AgP₂ (Fig. S12). Additionally, element mapping showed a uniform distribution of P on the surface of the nanowires with a mass ratio of 2.9 % (Fig. S13). These results demonstrated that the surface of Ag nanowires was transformed into AgP₂ by forming a typical core-shell structure of Ag@AgP₂, which well explained the increased diameter of the core after phosphating treatment. Similarly, the Ag@AgP₂ heterojunctions can also be found in the Ag@AgP₂@Ni-CoP@C sample. As displayed in Fig. 3f, a typical high-resolution TEM image showed clear heterogeneous interfaces among the Ni-doped CoP, Ag and AgP₂. Specifically, the lattice fringes with interplanar spacings of 2.35 and 1.46 Å can be assigned to the (111) and (024) planes of Ag and AgP₂, respectively (Fig. 3g-h). The TEM image in Fig. 3i confirmed the existence of Ag@AgP₂ heterojunction structure. While the lattice fringes with an interplanar spacing of 2.46 Å corresponded to the (111) crystal plane of Ni-doped CoP (Fig. 3j). The synergistical integrations of Ni-doped CoP nanoparticles and Ag@AgP₂ not only enhance the conductivity of the catalyst but also improve mass/charge transport. Furthermore, the core of Ag@AgP₂ effectively prevents the aggregations of Ni-doped CoP

nanostructures, which therefore increased the surface area of the catalysts and facilitated the exposure of catalytic active sites. These advantages effectively reduce the NRR reaction barrier for better NH₃ yields and FE. The diffraction rings in the SAED pattern correspond to the (200) and (102) crystal planes of Ag and CoP, respectively (Fig. 3k). Furthermore, element mapping analysis was performed to investigate the elemental distribution within the nanowires (Fig. 3l). The results revealed a concentrated distribution of Ag at the core of the nanowires, while Ni, Co, P, and C were uniformly distributed in the outer shell. This indicates the successful doping of Ni into CoP, and the uniform loading of CoP onto the Ag@AgP₂ nanowires. In addition, a linear composition scan along the cross-section of the nanowires was performed, and the results were consistent with the element mapping testing (Fig. S14). The mass percentages of Ag, Co, P, and Ni were determined to be 63.19 %, 14.35 %, 18.38 %, and 4.08 % by ICP-OES, respectively (Tab. S1). The above results demonstrated the successful preparation of Ag@AgP₂@Ni-CoP@C heterostructured nanowires.

The phase and crystal structure of the Ag@AgP₂@Ni-CoP@C catalyst was also characterized by XRD measurement. Fig. 4a showed that only four strong diffraction peaks can be observed, which corresponded to the (111), (200), (220), and (311) planes of Ag, respectively. Upon

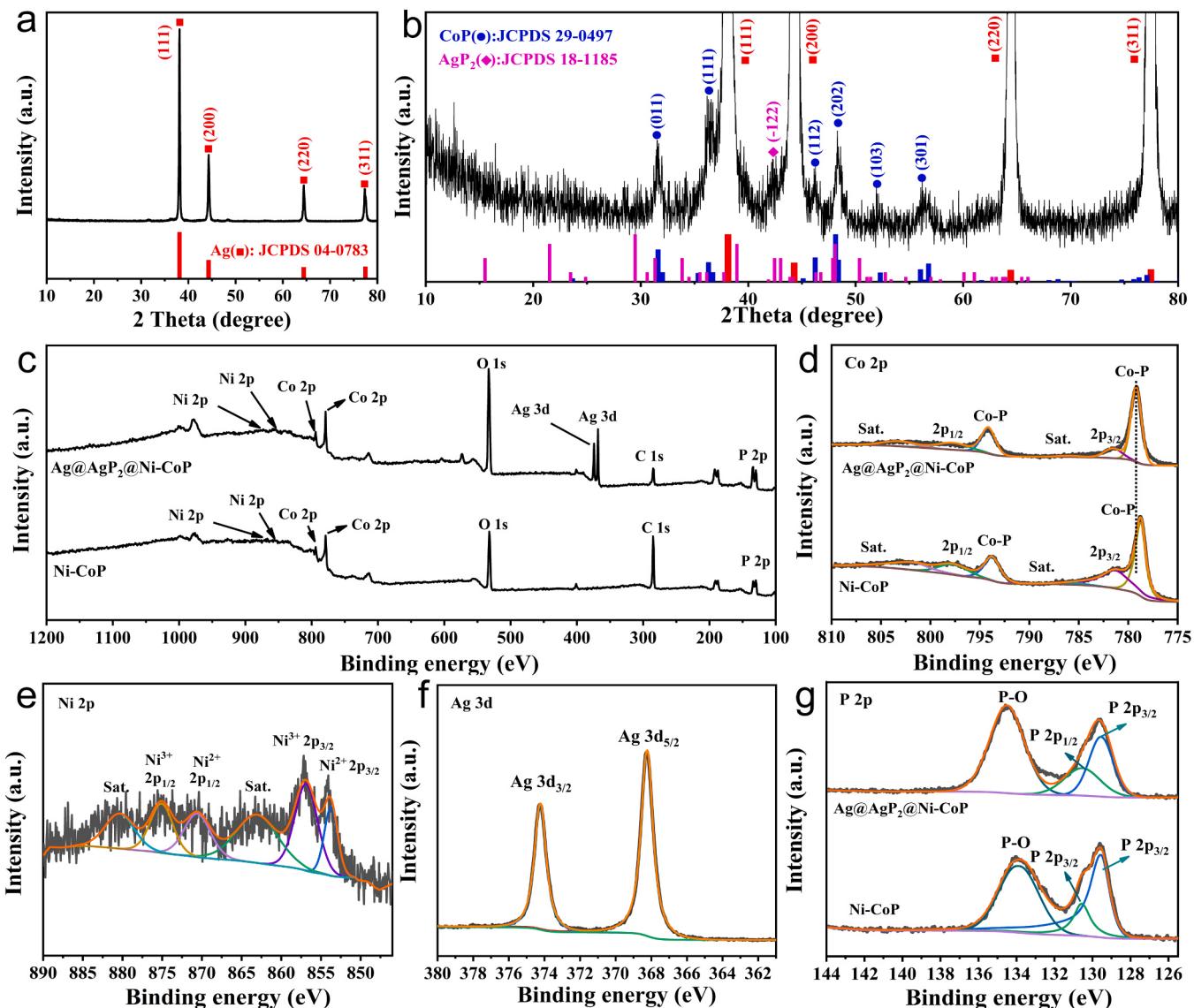


Fig. 4. XRD patterns (a, b) of the as-obtained Ag@AgP₂@Ni-CoP@C sample. High-resolution XPS spectrum of the as-fabricated Ni-doped CoP and Ag@AgP₂@Ni-CoP@C samples: (c) survey; (d) Ni 2p; (e) Co 2p; (f) Ag 3d and (g) P 2p.

magnification of the XRD pattern, as shown in Fig. 4b, weak peaks were detected at 2θ values of 31.7° , 36.3° , 46.3° , 48.3° , 52.1° , and 56.4° , corresponding to the (011), (111), (112), (202), (103), and (301) crystal planes of CoP (JCPDS No. 29-0497), respectively. Additionally, a peak was observed at a 2θ angle of 42.4° , which can be attributed to the (-122) plane of AgP₂ (JCPDS No. 18-1185). These results implied that the Ni-ZIF-67-based intermediate was completely transformed into Ni-doped CoP and the surface of Ag nanowires was converted into AgP₂ simultaneously. To further investigate the elemental states and chemical

bonding configurations of the Ag@AgP₂@Ni-CoP@C catalyst, X-ray photoelectron spectroscopy (XPS) measurements was conducted. The XPS spectrum of the Ni-doped CoP sample was also measured for comparison. As displayed in Fig. 4c, the elements Ag, Co, Ni, P, C and O were detected in the survey spectrum. The high-resolution spectrum of Co 2p consisted of two spin-orbit double peaks and two vibration satellite peaks (Fig. 4d). The two strong peaks at approximately 779.16 and 794.14 eV corresponded to the 2p_{3/2} and 2p_{1/2} energy levels of CoP because of spin orbit splitting, while the two strong peaks at 781.53 and

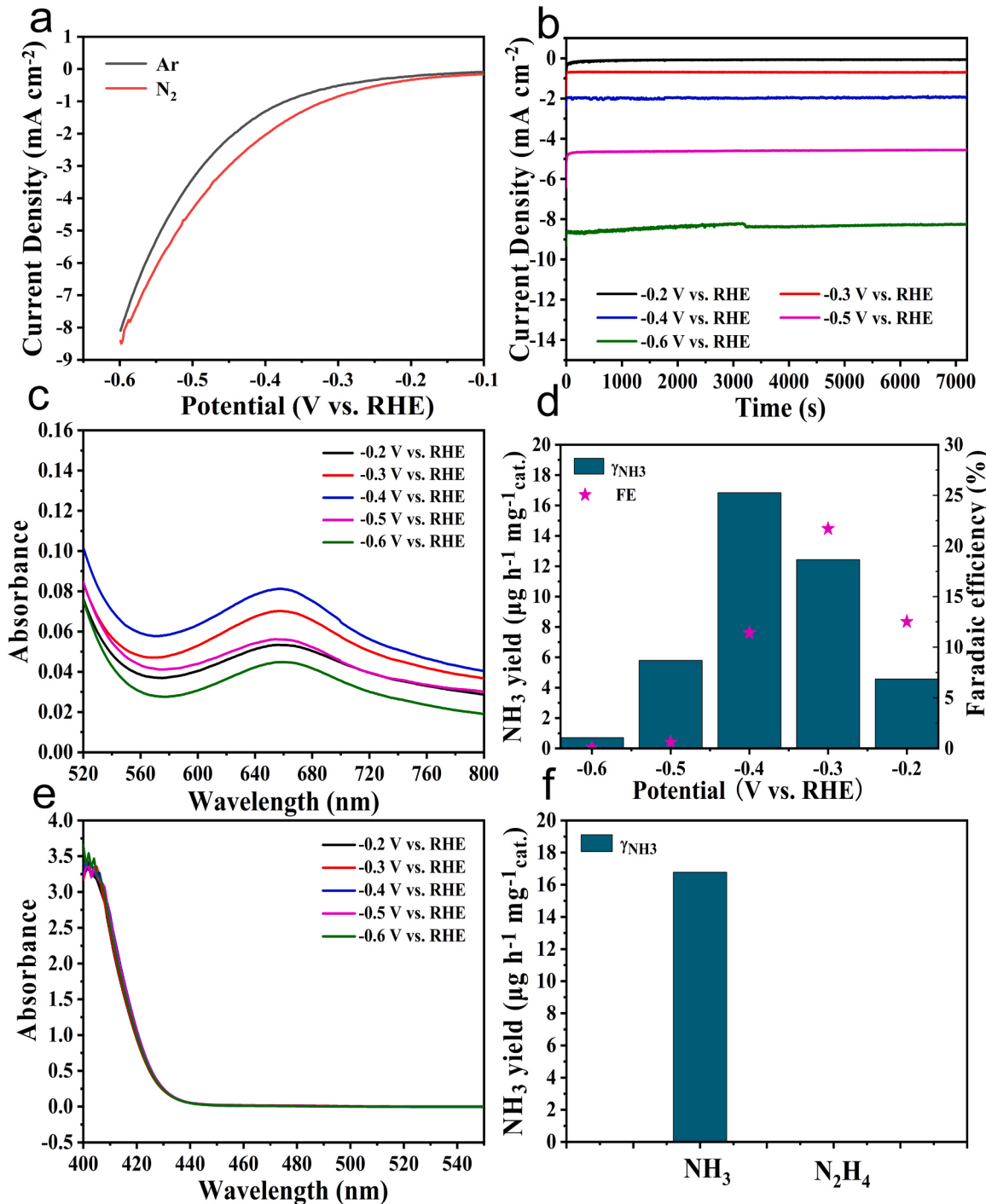


Fig. 5. (a) LSV curves of Ag@AgP₂@Ni-CoP@C in Ar and N₂ saturated 0.10 M Na₂SO₄. (b) Chronoamperometry curves of Ag@AgP₂@Ni-CoP@C under different potentials. (c) UV-Vis spectra of the electrolytes after test under different potentials. (d) γ_{NH_3} and FE of Ag@AgP₂@Ni-CoP@C under different potentials. (e) UV-Vis spectra of the electrolytes stained with p-C₉H₁₁NO indicator after NRR electrolysis at a series of potentials. (f) The NH₃ yield and hydrazine generated during electrochemical NRR at -0.4 V vs RHE.

797.88 eV corresponded to the $2p_{3/2}$ and $2p_{1/2}$ energy levels of Co-O bands, respectively. Besides, the peaks at 786.03 and 803.19 eV can be assigned to the satellite peaks (Sat.) [17,35]. Notably, the binding energy of Co 2p in the Ag@AgP₂@Ni-CoP@C was found to be positively shifted compared to the Ni-doped CoP sample, suggesting strong electron coupling effect between AgP₂ and Ni-CoP [36]. The high-resolution Ni 2p spectrum for Ag@AgP₂@Ni-CoP@C can be deconvoluted fitted into six peaks (Fig. 4e), in which the two peaks at 853.75 eV and 870.57 eV can be assigned to Ni 2p_{3/2} and Ni 2p_{1/2} of Ni²⁺ and the other two peaks at 856.82 eV and 875.09 eV can be attributed to the 2p_{3/2} and 2p_{1/2} energy levels of Ni³⁺ [37]. The low signal-to-noise ratio of the Ni peak suggests a low Ni content in the sample. The presence of Ni³⁺ is probably caused by the surface oxidation of the catalyst when exposed to ambient air [38]. The high-resolution spectrum of the Ag 3d region revealed two significant peaks at 368.44 eV (Ag 3d_{5/2}) and 374.47 eV (Ag 3d_{3/2}), which correspond to the Ag⁺ (Fig. 4f). The high-resolution spectrum of P exhibited two peaks at 129.56 eV and 130.56 eV, corresponding to the binding energies of P 2p_{3/2} and P 2p_{1/2}, respectively (Fig. 4g). A relatively wide peak at 134.50 eV corresponded to P-O species resulting from surface oxidation. The XPS results are consistent with the XRD, HRTEM and SAED pattern results, confirming the successful synthesis of Ag@AgP₂@Ni-CoP@C nanocomposites.

To evaluate the NRR performance of the prepared samples, a calibration curve of ammonia in 0.10 M Na₂SO₄ was first established using the spectrophotometric indoxyl blue method. Ammonium chloride solution with a known concentration was used as the standard solution, and the absorbance at 655 nm was measured by UV-Vis spectrophotometer after the standard solution was stained with indophenol for 2 h. The resulting UV-Vis curve and calibration curve for estimating ammonia concentration are shown in Fig. S15a and S15b, respectively. Additionally, to test the concentration of the N₂H₄ byproduct that may be produced during the NRR reaction, a calibration curve of N₂H₄ in 0.10 M Na₂SO₄ was also generated using Watt and ChrisP spectrophotometry. The standard solution was stained with the P-C₉H₁₁NO indicator and left at room temperature for 10 mins, resulting in the UV-Vis curves and calibration curves for calculating N₂H₄ concentrations shown in Fig. S16a and S16b, respectively.

To preliminarily verify the NRR activity of the Ag@AgP₂@Ni-CoP@C, linear sweep voltammetry (LSV) measurements were alternately conducted in 0.10 M Na₂SO₄ electrolyte saturated with either Ar or N₂. As shown in Fig. 5a, the Ag@AgP₂@Ni-CoP@C catalyst displayed cathode current in both electrolytes, indicating the presence of hydrogen evolution reaction during the test. However, a higher current density was observed in the N₂-saturated electrolyte, implying a greater contribution of the electrochemical conversion of N₂ into NH₃ [39]. The polarization curves in N₂ and Ar tended to converge gradually with the intense HER-dominated electrode process as the bias voltage became more negative [40]. Based on the polarization curve, the potential range suitable for electrochemical synthesis of NH₃ was defined as –0.1 to –0.6 V vs. RHE. The NRR catalytic activity of Ag@AgP₂@Ni-CoP@C was further evaluated in N₂-saturated Na₂SO₄ electrolyte using a H-type electrolytic cell. The relationship between current density and time (i-t curve) at different constant potentials for 2 h was recorded, as shown in Fig. 5b. The current density hardly fluctuated at different potentials during the 2-h electrolytic process, indicating good durability of the catalysts during the continuous electrolytic NRR processes. The electrolytes in the cathodic chamber were collected to quantitatively determine the NH₃ yield by the indophenol blue method. The corresponding UV-vis spectra were shown in Fig. 5c, with the absorbance reaching its maximum value at a potential of –0.4 V vs. RHE, suggesting that the NH₃ yield was at its highest. Based on the accumulated charge and the produced NH₃ concentration of electrolytes in the anodic chamber and cathodic chamber, the NH₃ yield rate and FE of Ag@AgP₂@Ni-CoP@C at various potentials can be determined. As shown in Fig. 5d, the maximum NH₃ yield was 16.84 µg h⁻¹ mg⁻¹_{cat} at a potential of –0.4 V vs. RHE, and the FE reached its highest value of 21.7 % at a

potential of –0.3 V vs. RHE. Notably, the NRR activity of Ag@AgP₂@Ni-CoP@C was superior to that of previously reported electrocatalysts in similar water-electrolyte systems (Tab. S2), such as PdZn/NHCP (5.28 µg h⁻¹ mg⁻¹_{cat}, 16.9 %) [41], Bi@C (4.22 µg h⁻¹ mg⁻¹_{cat}, 15.1 %) [42], WS₂/WO₂ (8.53 µg h⁻¹ mg⁻¹_{cat}, 13.5 %) [43], OVs-BiVO₄ (8.6 µg h⁻¹ mg⁻¹_{cat}, 10.4 %) [44], Pd-Ag-S PNSs (9.73 µg h⁻¹ mg⁻¹_{cat}, 18.4 %) [45]. However, when the potential was more negative than –0.4 V vs. RHE, HER gradually dominated, which blocked the surface-active sites and impeded the electrochemical NRR process, leading to the significantly decreased NH₃ yield [46]. The analysis of the by-product N₂H₄ concentration revealed that almost no N₂H₄ was detected in the electrolyzed solution (Fig. 5e-f), indicating the excellent selectivity of Ag@AgP₂@Ni-CoP@C for NH₃ production.

To elucidate the influence of Ni-doping and interface engineering on catalytic activity, CoP, Ni-CoP, Ag@AgP₂ and Ag@AgP₂@CoP@C catalysts were prepared as controls, and their performances were investigated in the same electrolyte. The XRD pattern shown in Fig. S17 confirmed the close match between the diffraction peaks of Ni-CoP and CoP, indicating the successful formation of Ni-CoP rather than NiCoP. TEM analysis in Fig. S18 revealed a porous and highly porous structure, suggesting its loose and porous nature. It was found the highest NH₃ yield was 9.23 µg h⁻¹ mg⁻¹_{cat} at a potential of –0.4 V vs. RHE and the highest FE was 8.93 % at –0.3 V vs. RHE (Fig. S19). In contrast, the NH₃ yield for CoP was only 6.7 µg h⁻¹ mg⁻¹_{cat}, with a FE of 8.3 % (Fig. S20). The NH₃ yield for Ag@AgP₂@CoP@C was 13.17 µg h⁻¹ mg⁻¹_{cat}, with a FE of 15.5 % (Fig. S21). These values are all lower than those obtained with Ag@AgP₂@Ni-CoP@C. These control experiments confirmed the positive impact of Ni doping on the NRR performance. To investigate the effect of Ni doping on the electronic band structure of CoP, DFT calculations were conducted. The crystal structure model of Ni-CoP from both top and side views is presented in Fig. S22a and b. It was observed that both CoP (Fig. S22c) and Ni-CoP (Fig. S22d) exhibited density of states (DOS) passing through the Fermi level (located at 0 eV), indicating the absence of a band gap and high conductivity in both materials. By comparing the total DOS (TDOS) in Fig. S22e and f, it was evident that Ni-CoP showed relatively increased charge density around the Fermi level compared to CoP. Consequently, the incorporation of Ni into CoP is expected to provide more charge carriers during the reaction, thereby leading to improved NRR performance. Moreover, the performance of Ag@AgP₂ was inferior to that of Ag@AgP₂@Ni-CoP@C (Fig. S23), underscoring the advantages of the synergistic effect in the multi-component system and the superiority of the designed materials.

To further investigate the origin of the improved NRR activity of Ag@AgP₂@Ni-CoP@C, the electrochemical surface area (ECSA) was estimated by measuring the double-layer capacitance (C_{dl}). The cyclic voltammetry at different scanning rates ranging from 20 to 100 mV s⁻¹ was displayed in Fig. S24. It was found that the C_{dl} of Ag@AgP₂@Ni-CoP@C was 10.3 mF cm⁻², while the C_{dl} of Ni-CoP was 8.64 mF cm⁻² (Fig. S24c and 24d). These results indicate that Ag@AgP₂@Ni-CoP@C exhibited a larger electrochemically active surface area. The high active surface area provided a larger number of active sites, which are favorable for electrocatalytic NRR activity. Additionally, the EIS spectrum showed that the Ag@AgP₂@Ni-CoP@C exhibited smaller semicircles compared to those of Ni-CoP and Ag@AgP₂ (Fig. S25), indicating lower charge transfer resistance in the presence of Ni-CoP nanoparticles. This can be closely associated with the modulated electronic structure and enhanced conductivity of CoP contributed by Ni-doping.

Durability and cycle stability are important factors that must be considered when evaluating the practicality of catalysts for applications. To assess these properties, a time-dependent current density curve was obtained for the catalysts in N₂-saturated electrolyte (Fig. 6a). The results showed that the catalysts were able to maintain a current density of –0.40 V vs. RHE for at least 12 h, indicating good stability and corrosion resistance. Additionally, the fluctuation in NH₃ yields and faradaic efficiencies of Ag@AgP₂@Ni-CoP@C during six cycles of testing was found to be minimal (Fig. 6b), suggesting that the catalysts were able to

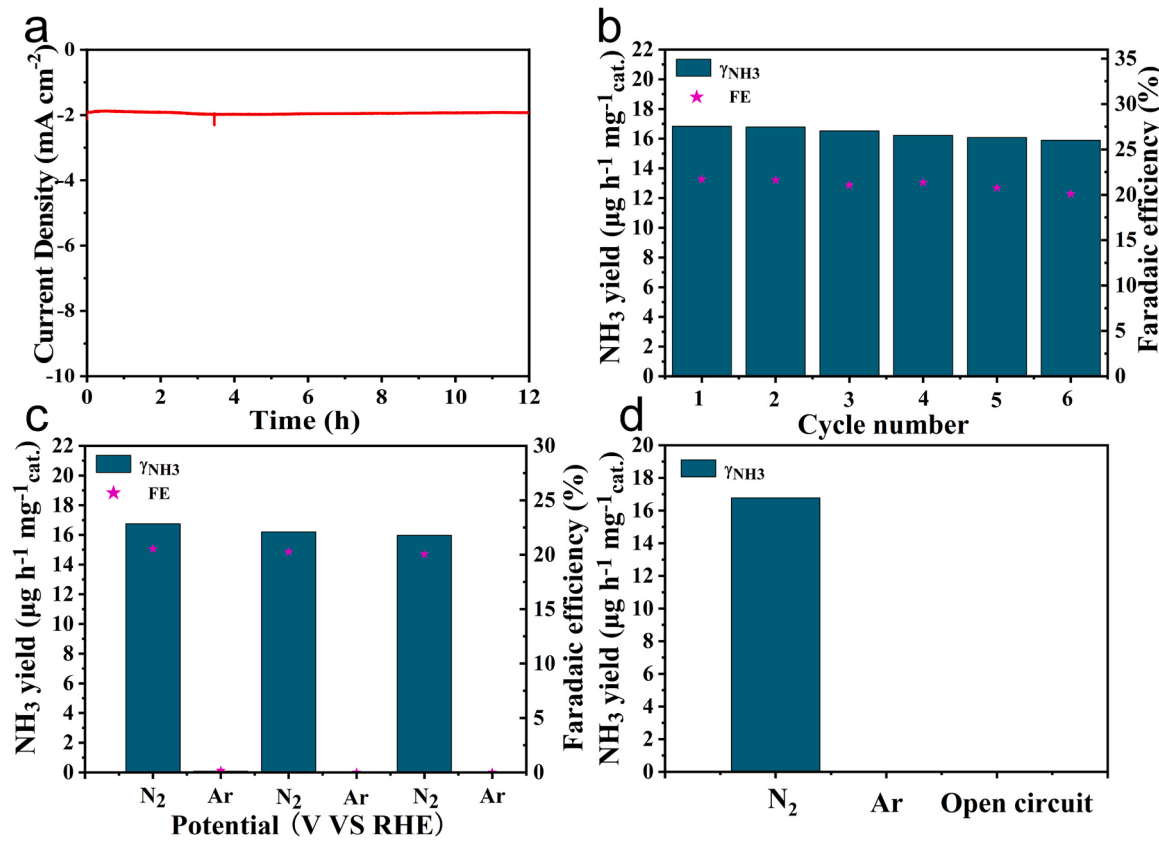


Fig. 6. Time-dependent current density curve (a) and recycling test (b) for Ag@AgP₂@Ni-CoP@C at the best potential. NH₃ yield and FEs (c) for alternating 2 h cycles in N₂/Ar-saturated electrolytes, respectively. NH₃ yields (d) in different gas-saturated Na₂SO₄ electrolytes and open circuit in N₂ after 2 h electrolysis for Ag@AgP₂ @Ni-CoP@C at -0.40 V vs. RHE.

maintain its initial catalytic activity over an extended period of time. After conducting the durability testing, XRD, TEM, and XPS characterization were performed to assess the stability and potential changes in the catalyst. XRD pattern in Fig. S26 indicated that there were no significant changes in the crystal structure. TEM image in Fig. S27 revealed that the core-shell morphology of the catalyst remained largely unchanged after the durability testing. Additionally, the high-resolution XPS spectrum for the Ag, Ni, Co and P elements before and after durability testing were compared, and no significant variations were observed (Fig. S28). This suggests that the surface elemental composition and valence states remained stable. These characterization results collectively demonstrate the durability and stability of the Ag@AgP₂@Ni-CoP@C, which makes it a promising candidate for practical applications.

To further demonstrate that the detected ammonia was produced via the NRR process using Ag@AgP₂ @Ni-CoP@C catalysts, a series of comparative experiments were conducted. Firstly, Ag@AgP₂@Ni-CoP@C catalysts were used to alternate between N₂-saturated and Ar-saturated electrolytes for NRR electrocatalysis in a 2 h cycle (Fig. 6c). The results showed that a significant NH₃ yield was observed in the N₂-saturated electrolyte, while almost no NH₃ was detected in the Ar-saturated electrolyte. This suggests that the production of NH₃ was directly linked to the NRR process, as the reaction requires the presence of N₂ gas. Secondly, the Ag@AgP₂ @Ni-CoP@C catalysts were maintained in the N₂-saturated electrolyte for 2 h, followed by electrocatalysis in the Ar-saturated electrolyte for 2 h, and then electrolysis at the open-circuit potential in the N₂-saturated electrolyte for 2 h (Fig. 6d). The results showed that NH₃ was only detected after electrolysis in the N₂-saturated electrolyte, implying that there was no contamination from external sources or the catalysts themselves. These findings further support the conclusion that NH₃ was produced

exclusively from the reduction of N₂ over Ag@AgP₂@Ni-CoP@C, rather than from external environmental pollution.

DFT calculations were then performed to examine the role of Ag, Ni-CoP, and AgP₂ in the enhanced activity and selectivity of the electrocatalytic ammonia synthesis. The effective adsorption and activation of N₂ on the catalyst surface is a crucial step for NRR. We have considered five possible adsorbed configurations for N₂ molecules, as depicted in Fig. 7a. These configurations include end-on adsorption of N₂ on a single

Ni site (I) or Co site (II), side-on adsorption of N₂ on a single Ni site (III) or Co site (IV), and bimetallic Ni&Co site (V). After structure optimization, it was found that the IV and V configurations are identical. The N-N bond lengths for the five configurations were 1.14, 1.13, 1.15, 1.17 and 1.17 Å, respectively, slightly longer than the N-N bond length of 1.12 Å in an isolated N₂ molecule. The longest N-N bond in the Ni&Co (V) adsorption configuration suggests better N₂ activation [47,48]. Besides, the adsorption energy of N₂ molecules for the Ni&Co (V) adsorption configuration is the most negative among the five models. These results suggest that the side-on configuration is more favorable thermodynamically than the end-on configuration. The difference in N₂ bond length elongation can be attributed to the different amounts of charge transfer from the catalyst to the N₂ molecule. According to Bader charge analysis, the charge transfer in the side-on configuration is 0.37e, which is more significant than the ones in the end-on configuration (Fig. 7b). Therefore, the significant elongation of the N-N bond in the side-on configuration is likely due to the greater charge transfer between catalyst and N₂. The charge density difference was also calculated to gain insight into the observed N₂ activation on the catalyst surface (Fig. 7c). It was found that the charge transfer is a "two-way" process, with N₂ adsorption following an "acceptance-donation" process: charge accumulation and depletion can be observed for both N₂ molecules and terminated Co atoms, with Co atoms accepting lone-pair electrons and

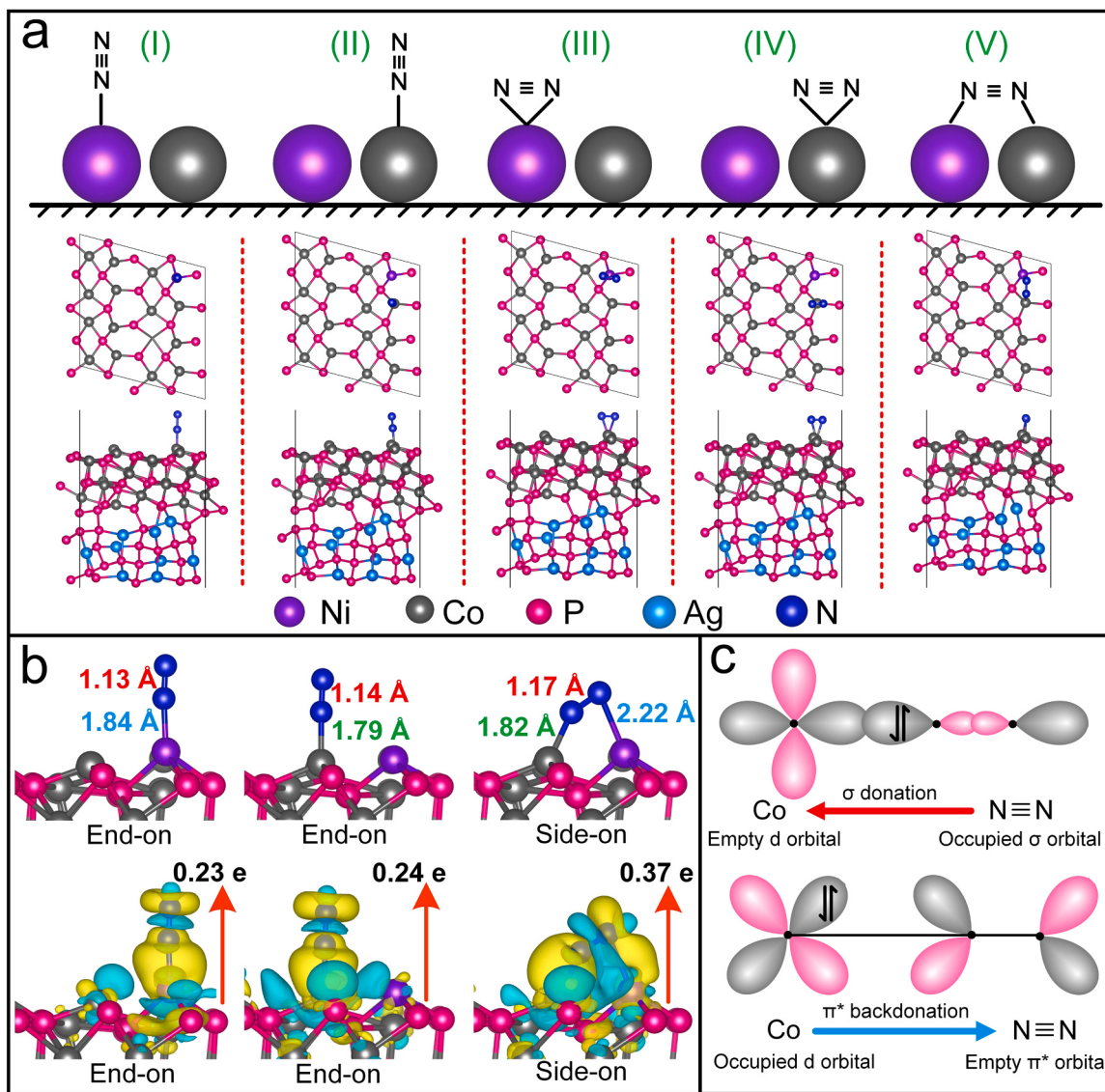


Fig. 7. (a) The scheme and geometric presentations for five possible N₂ adsorption modes on the surface of Ni-Co-P heterojunctions. The charge density differences (b) on the surface of Ag@AgP₂@Ni-CoP@C catalyst via side-on pattern and end-on pattern. The values in red, blue and green are the bond length of N-N, Ni-N and Co-N, respectively. (c) Schematics of N₂ bonding to the as electrocatalyst.

simultaneously donating electrons to the anti-bonding orbitals of N₂ [49]. This process is confirmed by comparing the projected density of states (PDOS) of the surface before and after N₂ adsorption (Fig. S29).

Generally, the nitrogen molecule can be reduced to ammonia through associative-involved mechanisms including the distal, alternating, and enzymatic pathways. These pathways all involve the formation of two NH₃ molecules through six steps of hydrogenation [50]. To evaluate the catalytic activity of Ag@AgP₂@Ni-CoP@C for the NRR, the free energy changes (ΔG) for each elementary step were investigated. Fig. 8a shows the computed Gibbs free energy diagrams for the enzymatic pathway, and the corresponding adsorbed species structures is displayed in Fig. 8b. Following the enzymatic pathway, the first hydrogenation step occurs when the H⁺/e⁻ couple attacks one N atom to form NNH* with a low free energy barrier of 0.64 eV. This step is the potential-determining step (PDS) for the entire NRR with a low limiting potential. The second H⁺/e⁻ couple then attacks the other N atom to form NHNH* with a downhill energy of 0.19 eV. In the third and fourth steps, the formed NHNH* species is further reduced to NHNHH* and NHNNHH*, respectively. In the fifth step, the N-N bond breaks with an energy release of 0.88 eV to form NHH* and an NH₃ molecule. In the last

two steps, an energy of 0.24 eV is required to form NH₃, and an energy of 0.55 eV is needed to release NH₃ molecules.

When the NRR proceeds through the distal pathways, the H⁺/e⁻ couple initiates the process by attacking the upper N atom, forming an NNH* intermediate (Fig. S30). Subsequently, a second pair of H⁺/e⁻ attacks the distal N atom, resulting in the formation of NNHH* species. The N-N bond then breaks upon further hydrogenation, releasing the first NH₃ molecule. An additional three hydrogenation steps are required for the release of the second NH₃ molecule. It is noteworthy that throughout this entire pathway, the N atom remains exclusively connected to one Co atom. The ΔG values for each step are 1.41, -0.27, 0.88, -0.57, -2.22, and -0.04 eV, respectively (Fig. 8c). For the alternating pathway, the structural configurations for each intermediate state are shown in Fig. S31, and the ΔG values for each step are 1.41, 0.02, -0.08, -0.56, -1.56, and -0.04 eV, respectively. Fig. S31 Based on the above calculation results, we can find that the PDS is located at the formation of N₂H species for distal and alternating pathway due to the maximum ΔG value of 1.41 eV, indicating that nitrogen reduction tends to occur through the enzymatic pathway.

As HER is a prevalent side-reaction against NRR, which can

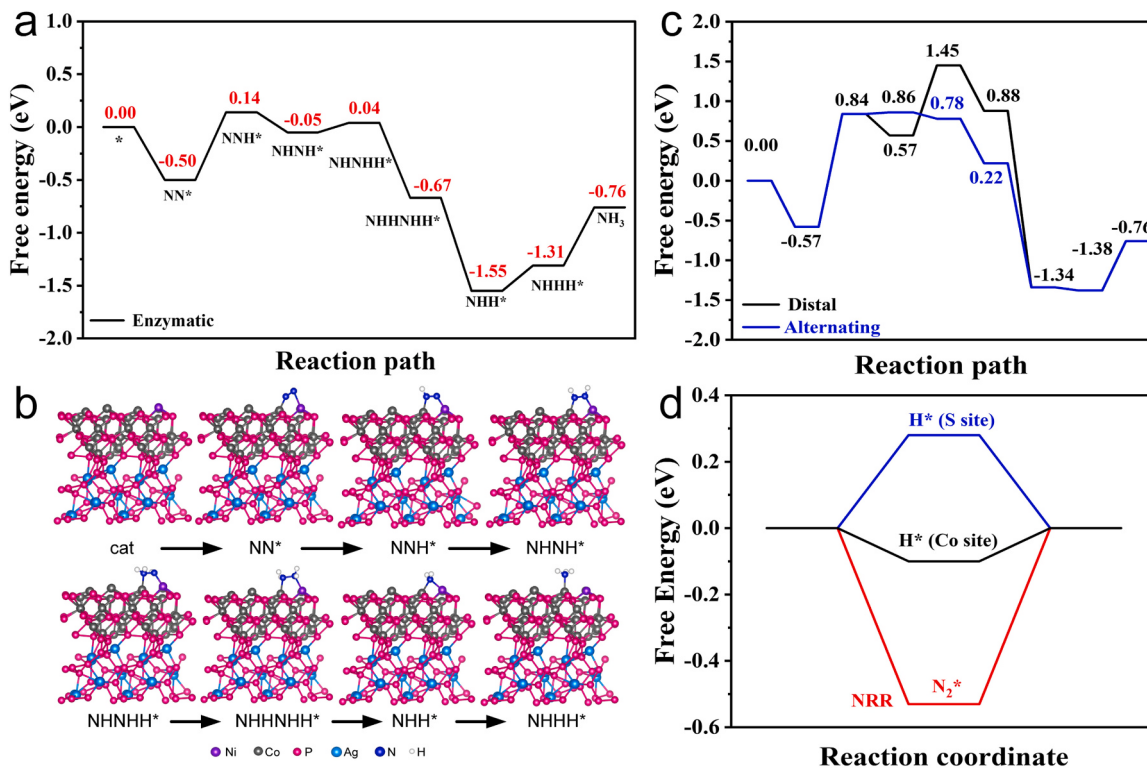


Fig. 8. The preferred Gibbs free energy diagrams (a) and corresponding adsorbed species structures (b) on AgP₂@Ni-CoP@C; (c) distal and alternating mechanisms; (d) Free energies for N₂ and H absorption on AgP₂@Ni-CoP@C (ΔG_{N2^*} and ΔG_{H^*}).

significantly decrease the Faradaic efficiency and current density of NRR. To evaluate the selectivity of the as-prepared Ag@AgP₂@Ni-CoP@C catalyst, a comparison of the free energy change associated with the adsorption of N₂^{*} and H^{*} was performed. Apparently, the value of ΔG_{N2^*} should be more negative than that of ΔG_{H^*} to ensure that the adsorption of N₂^{*} is favored over that of H^{*} on the catalytic surface, thus preventing the inhibition of N₂ chemisorption by the adsorption of H^{*} [51]. As illustrated in Fig. 8d, the free energy change associated with H^{*} adsorption (ΔG_{H^*}) on Ag@AgP₂@Ni-CoP@C is more positive than that of N₂^{*} adsorption (ΔG_{N2^*}), with values of -0.1 eV (Co site) and 0.28 eV (P site) compared to -0.53 eV for ΔG_{N2^*} . This indicates that Ag@AgP₂@Ni-CoP is more favorable for the adsorption of N₂ over H during the catalytic process. This feature can significantly suppress the competing HER, thereby endowing the as-synthesized Ag@AgP₂@Ni-CoP catalyst with high activity and selectivity towards NRR.

To further illustrate the advantages of interface engineering in catalyzing the reduction of inert N₂ gas, the DOS was subsequently conducted to analyze the structural features of the as-synthesized Ag@AgP₂@Ni-CoP@C heterostructured nanowires. The DOS analysis revealed that, compared to pure CoP, the Ag@AgP₂@Ni-CoP@C exhibits a significant increase in electron density at the Fermi level (Fig. S32), with contributions from Co, Ag and P, which is believed to play a key role in the improved NRR performance. To understand the origin of the increase in electron density, the deformation charge density diagram of the AgP₂/Ni-CoP heterostructure was analyzed. This analysis showed that electrons transfer from Ni-doped CoP to AgP₂, resulting in electron-deficient regions near Ni-doped CoP and electron-rich regions near AgP₂ (Fig. S33). These findings were consistent with the XPS results and the calculated work functions (Fig. S34). The presence of electron-deficient regions near Ni-doped CoP allows for the acceptance of lone-pair electrons from N₂, reducing the N₂ adsorption energy and promoting N₂ adsorption. This, in turn, significantly enhances NRR kinetics. The electron-rich regions near AgP₂, on the other hand, are able to transfer accumulated electrons to the empty N₂

antibonding orbital, facilitating the cleavage of N-N triple bonds and contributing to the overall NRR performance [25]. To further understand the electronic structure of the samples, PDOS was calculated for the Co atoms in the CoP and the interface of Ni-CoP/AgP₂. The PDOS analysis revealed that the d-band center of interfacial Co atoms shifts upward (closer to the Fermi level) compared to Co atoms in pure CoP (Fig. S35). This shift is believed to be responsible for the enhanced N₂ chemisorption and NRR activity observed in the Ag@AgP₂@Ni-CoP@C catalyst. These changes are reflected in the increase in N₂ adsorption energy and the decrease in the hydrogenation reaction energy barrier, both of which contribute to the improved NRR performance of the catalyst [52].

Based on the electrochemical characterization and DFT calculation results, the as-synthesized Ag@AgP₂@Ni-CoP@C catalyst indeed displayed excellent electrocatalytic activity, selectivity, and durability for NRR. This superior performance can mainly be attributed to the following features: (1) The unique porous shell structures provide more surface area for the materials, thus providing sufficient active sites to promote the electrolyte penetration and transport. (2) Ag nanowires effectively improve the electrical conductivity of the catalyst and enhance the electrochemical stability of the electrode. Meanwhile, the Ag@AgP₂ nanowires as core effectively prevent the agglomeration of the Ni-doped CoP nanoparticles; (3) The formed heterojunctions between Ni-CoP and AgP₂ not only increase the exposure of highly active sites but also induce the redistribution of electrons around active centers, which effectively enhance charge transportation and tailor the chemisorption free energies of the NRR intermediates.

4. Conclusions

In summary, we have successfully synthesized Ag@AgP₂@Ni-CoP@C core-shell nanowires as an efficient catalyst for NRR. The merging of conductive Ag core with porous and active Ni-doped CoP shell results in robust heterostructured nanowires that favor both the

mass transfer from the electrolyte to the electrodes and the electron transfer to the active sites, thus effectively lowering the activation energy toward the reduction of N₂ to NH₃. As a result of these advantages, the Ag@AgP₂@Ni-CoP@C nanowires showed excellent NRR performance, including high NH₃ yield, high Faradaic efficiency, and long-term durability. The maximum NH₃ yield is 16.84 μg h⁻¹ mg_{cat}⁻¹ at -0.4 V vs. RHE, and the highest Faradaic efficiency is 21.7 % at -0.3 V vs. RHE. Our strategy for constructing this NRR electrocatalyst is a promising approach for future research in electrocatalysis and could potentially be applied to the production of nitrogen-containing compounds for various industrial and environmental purposes.

CRediT authorship contribution statement

Shoushuang Huang and **Zhangjun Hu** contributed to the experimental Conceptualization, investigation, electrochemical measurement, and Writing – original draft. **Jinmei Bao** and **Deyu Xiang** conducted materials characterizations and contributed to the Writing – review & editing. **Chunyan Gao** and **Shuzhen Ma** contributed to the electrochemical measurements. **Qiaochuan Chen** contributed to the Software and Writing – original draft. **Kaimei Peng** and **Yong Jiang** were involved in the experimental Conceptualization, provided Resources, and contributed to the Writing – review & editing. **Jiujun Zhang** contributed to the experimental Conceptualization and provided review and editing support. All authors actively participated in discussions regarding the results and provided valuable comments on the manuscript.

Declaration of Competing Interest

The authors declare that they have no known competing financial interests or personal relationships that could have appeared to influence the work reported in this paper.

Data availability

Data will be made available on request.

Acknowledgements

The work was financially supported by the National Natural Science Foundation of China (12275168), Science and Technology Innovation Plan of Shanghai Science and Technology Commission (21010500300), Guizhou Provincial Science and Technology Foundation (No. [2020] 1Y043), STINT Joint China-Sweden Mobility Project (CH2017-7243), and Swedish Government Strategic Research Area in Materials Science on Advanced Functional Materials at Linköping University (SFO-MatLiU, No. 2009 0097).

Appendix A. Supporting information

Supplementary data associated with this article can be found in the online version at [doi:10.1016/j.apcatb.2023.122998](https://doi.org/10.1016/j.apcatb.2023.122998).

References

- [1] C.J.M. van der Ham, M.T.M. Koper, D.G.H. Hetterscheid, Challenges in reduction of dinitrogen by proton and electron transfer, *Chem. Soc. Rev.* 43 (2014) 5183–5191.
- [2] X. Zhao, G. Hu, G.F. Chen, H. Zhang, S. Zhang, H. Wang, Comprehensive understanding of the thriving ambient electrochemical nitrogen reduction reaction, *Adv. Mater.* 33 (2021), 2007650.
- [3] S. Zhao, X. Lu, L. Wang, J. Gale, R. Amal, Carbon-based metal-free catalysts for electrocatalytic reduction of nitrogen for synthesis of ammonia at ambient conditions, *Adv. Mater.* 31 (2019), 1805367.
- [4] J. Deng, J.A. Iniguez, C. Liu, Electrocatalytic nitrogen reduction at low temperature, *Joule* 2 (2018) 846–856.
- [5] L. Shi, Y. Yin, S.B. Wang, H.Q. Sun, Rational catalyst design for n2 reduction under ambient conditions: strategies toward enhanced conversion efficiency, *ACS Catal.* 10 (2020) 6870–6899.
- [6] G.F. Chen, S. Ren, L. Zhang, H. Cheng, Y. Luo, K. Zhu, L.X. Ding, H. Wang, Advances in electrocatalytic N₂ reduction-strategies to tackle the selectivity challenge, *Small Methods* 3 (2018), 1800337.
- [7] Y.W. Ren, C. Yu, X.Y. Tan, H.L. Huang, Q.B. Wei, J.S. Qiu, Strategies to suppress hydrogen evolution for highly selective electrocatalytic nitrogen reduction: challenges and perspectives, *Energy Environ. Sci.* 14 (2021) 1176–1193.
- [8] C.Y. Guo, X.J. Liu, L.F. Gao, X. Kuang, X. Ren, X.J. Ma, M.Z. Zhao, H. Yang, X. Sun, Q. Wei, Fe-doped Ni₂P nanosheets with porous structure for electroreduction of nitrogen to ammonia under ambient conditions, *Appl. Catal. B Environ.* 263 (2020), 118296.
- [9] Y. Deng, Z.Y. Xiao, Z.C. Wang, J.P. Lai, X.B. Liu, D. Zhang, Y. Han, S.X. Li, W. Sun, L. Wang, The rational adjusting of proton-feeding by Pt-doped Fe₂C hollow nanorod for promoting nitrogen reduction kinetics, *Appl. Catal. B Environ.* 291 (2021), 120047.
- [10] L. Zhang, X.Q. Ji, X. Ren, Y.J. Ma, X.F. Shi, Z.Q. Tian, A.M. Asiri, L. Chen, B. Tang, X.P. Sun, Electrochemical ammonia synthesis via nitrogen reduction reaction on a MoS₂ catalyst: theoretical and experimental studies, *Adv. Mater.* 30 (2018), 1800191.
- [11] K. Chu, Y.P. Liu, Y.B. Li, H. Zhang, Y. Tian, Efficient electrocatalytic N₂ reduction on CoO quantum dots, *J. Mater. Chem. A* 7 (2019) 4389–4394.
- [12] Z. Xi, K. Shi, X. Xu, P. Jing, B. Liu, R. Gao, J. Zhang, Boosting nitrogen reduction reaction via electronic coupling of atomically dispersed bismuth with titanium nitride nanorods, *Adv. Sci.* 9 (2022), 2104245.
- [13] Z. Ma, J. Chen, D. Luo, T. Thersleff, R. Dronskowski, A. Slabon, Structural evolution of CrN nanocube electrocatalysts during nitrogen reduction reaction, *Nanoscale* 12 (2020) 19276–19283.
- [14] Q.F. Yao, J.B. Chen, S.Z. Xiao, Y.L. Zhang, X.F. Zhou, Selective electrocatalytic reduction of nitrate to ammonia with nickel phosphide, *ACS Appl. Mater. Interfaces* 13 (2021) 30458–30467.
- [15] Q.G. Meng, Y.P. Hou, F.Q. Yang, C.L. Cao, Z. Zou, J.H. Luo, W.Z. Zhou, Z.K. Tong, S.X. Chen, S.D. Zhou, J. Wang, S.G. Deng, Modulation of surface properties on cobalt phosphide for high-performance ambient ammonia electrosynthesis, *Appl. Catal. B Environ.* 303 (2022), 120874.
- [16] W.H. Guo, Z.B. Liang, J.L. Zhao, B.J. Zhu, K.T. Cai, R.Q. Zou, Q. Xu, Hierarchical cobalt phosphide hollow nanocages toward electrocatalytic ammonia synthesis under ambient pressure and room temperature, *Small Methods* 2 (2018), 1800204.
- [17] S.H. Ye, Z.D. Chen, G.K. Zhang, W.D. Chen, C. Peng, X.Y. Yang, L.R. Zheng, Y.L. Li, X.Z. Ren, H.Q. Cao, D.F. Xue, J.S. Qiu, Q.L. Zhang, J.H. Liu, Elucidating the activity, mechanism and application of selective electrosynthesis of ammonia from nitrate on cobalt phosphide, *Energy Environ. Sci.* 15 (2022) 760–770.
- [18] Y. Liu, X.R. Zhu, Q.H. Zhang, T. Tang, Y. Zhang, L. Gu, Y.F. Li, J.C. Bao, Z.H. Dai, J. S. Hu, Engineering Mo/Mo₂C/MoC hetero-interfaces for enhanced electrocatalytic nitrogen reduction, *J. Mater. Chem. A* 8 (2020) 8920–8926.
- [19] J.L. Lv, Z.F. Tian, K. Dai, Y.X. Ye, C.H. Liang, Interface and defect engineer of titanium dioxide supported palladium or platinum for tuning the activity and selectivity of electrocatalytic nitrogen reduction reaction, *J. Colloid Interface Sci.* 553 (2019) 126–135.
- [20] J.B. Hou, M. Yang, J.L. Zhang, Recent advances in catalysts, electrolytes and electrode engineering for the nitrogen reduction reaction under ambient conditions, *Nanoscale* 12 (2020) 6900–6920.
- [21] T. Ye, K. Ba, X.Y. Yang, T.S. Xiao, Y.Y. Sun, H.Q. Liu, C. Tang, B.H. Ge, P. Zhang, T. Duan, Z.Z. Sun, Valence engineering at the interface of MoS₂/Mo₂C heterostructure for bionic nitrogen reduction, *Chem. Eng. J.* 452 (2023), 139515.
- [22] T.Y. Jiang, L.X. Li, L.H. Li, Y.H. Liu, D.X. Zhang, D.Q. Zhang, H.T. Li, B.D. Mao, W. D. Shi, Ultra-thin shelled Cu_{2-x}S/MoS₂ quantum dots for enhanced electrocatalytic nitrogen reduction, *Chem. Eng. J.* 426 (2021), 130650.
- [23] J.Z. Qin, X. Hu, X.Y. Li, Z.F. Yin, B.J. Liu, K. Lam, OD/2D AgInS₂/MXene Z-scheme heterojunction nanosheets for improved ammonia photosynthesis of N₂, *Nano Energy* 61 (2019) 27–35.
- [24] H. Huang, F. Gong, Y. Wang, H.B. Wang, X.F. Wu, W.B. Lu, R.B. Zhao, H.Y. Chen, X.F. Shi, A.M. Asiri, T.S. Li, Q. Liu, X.P. Sun, Mn₃O₄ nanoparticles@reduced graphene oxide composite: an efficient electrocatalyst for artificial N₂ fixation to NH₃ at ambient conditions, *Nano Res.* 12 (2019) 1093–1098.
- [25] S.H. Liu, G.H. Yang, L. Zhao, Z.P. Liu, K.W. Wang, X.T. Li, N. Li, 1T-MoS₂ nanosheets coupled with cos₂ nanoparticles: electronic modulation for efficient electrochemical nitrogen fixation, *Inorg. Chem.* 61 (2022) 7608–7616.
- [26] D.P. Chen, X.L. Qiao, X.L. Qiu, J.Z. Chen, R.Z. Jiang, Large-scale synthesis of silver nanowires via a solvothermal method, *J. Mater. Sci. Mater. Electron.* 22 (2010) 6–13.
- [27] D. Zhu, L.H. Zhang, R.E. Ruther, R.J. Hamers, Photo-illuminated diamond as a solid-state source of solvated electrons in water for nitrogen reduction, *Nat. Mater.* 12 (2013) 836–841.
- [28] T. Dambruskaas, H. Cornish, A modified spectrophotometric method for the determination of hydrazine, *Am. Ind. Hyg. Assoc. J.* 23 (1962) 151–156.
- [29] K. Kim, S. Baek, J.J. Kim, J.W. Han, Catalytic decomposition of N₂O on Pd Cu alloy catalysts: a density functional theory study, *Appl. Surf. Sci.* 510 (2020), 145349.
- [30] Z.X. Wei, J. He, Y.L. Yang, Z.H. Xia, Y.Z. Feng, J.M. Ma, Fe, V-co-doped C₂N for electrocatalytic N₂-to-NH₃ conversion, *J. Energy Chem.* 53 (2021) 303–308.
- [31] J.L. Gu, L. Sun, Y.X. Zhang, Q.Y. Zhang, X.W. Li, H.C. Si, Y. Shi, C. Sun, Y. Gong, Y. H. Zhang, MOF-derived Ni-doped CoP@C grown on CNTs for high-performance supercapacitors, *Chem. Eng. J.* 385 (2020), 123454.
- [32] P.P. Wei, H.T. Xie, X.J. Zhu, R.B. Zhao, L. Ji, X. Tong, Y.S. Luo, G.W. Cui, Z. M. Wang, X.P. Sun, Co₂ nanoparticles-embedded N-doped carbon nanobox

- derived from ZIF-67 for electrocatalytic N₂-to-NH₃ fixation under ambient conditions, *ACS Sustain. Chem. Eng.* 8 (2019) 29–33.
- [33] S.S. Huang, Z.Q. Jin, Y.W. Ding, P. Ning, Q.C. Chen, J. Fu, Q. Zhang, J. Zhang, P. J. Xin, Y. Jiang, Z.J. Hu, Encapsulating Fe₂O₃ nanotubes into carbon-coated Co₉S₈ nanocages derived from a MOFs-directed strategy for efficient oxygen evolution reactions and Li-ions storage, *Small* 17 (2021), 2103178.
- [34] H. Hu, B.Y. Guan, B.Y. Xia, X.W. Lou, Designed formation of Co₃O₄/NiCo₂O₄ double-shelled nanocages with enhanced pseudocapacitive and electrocatalytic properties, *J. Am. Chem. Soc.* 137 (2015) 5590–5595.
- [35] S.H. Ye, W. Xiong, P. Liao, L.R. Zheng, X.Z. Ren, C.X. He, Q.L. Zhang, J.H. Liu, Removing the barrier to water dissociation on single-atom Pt sites decorated with a CoP mesoporous nanosheet array to achieve improved hydrogen evolution, *J. Mater. Chem. A* 8 (2020) 11246–11254.
- [36] H. Su, K.X. Zhang, B. Zhang, H.H. Wang, Q.Y. Yu, X.H. Li, M. Antonietti, J.S. Chen, Activating cobalt nanoparticles via the Mott-Schottky effect in nitrogen-rich carbon shells for base-free aerobic oxidation of alcohols to esters, *J. Am. Chem. Soc.* 139 (2017) 811–818.
- [37] S.S. Huang, Q. Zhang, P.J. Xin, J. Zhang, Q.C. Chen, J. Fu, Z.Q. Jin, Q. Wang, Z. J. Hu, Construction of Fe-doped NiS-NiS₂ heterostructured microspheres via etching prussian blue analogues for efficient water-urea splitting, *Small* 18 (2022), 2106841.
- [38] P. Thangasamy, S. Oh, S. Nam, H. Randriamahazaka, I.K. Oh, Ferrocene-Incorporated cobalt sulfide nanoarchitecture for superior oxygen evolution reaction, *Small* 16 (2020), 2001665.
- [39] X.X. Chen, Y.T. Liu, C.L. Ma, J.Y. Yu, B. Ding, Self-organized growth of flower-like SnS₂ and forest-like ZnS nanoarrays on nickel foam for synergistic superiority in electrochemical ammonia synthesis, *J. Mater. Chem. A* 7 (2019) 22235–22241.
- [40] J. Wang, L. Yu, L. Hu, G. Chen, H.L. Xin, X.F. Feng, Ambient ammonia synthesis via palladium-catalyzed electrohydrogenation of dinitrogen at low overpotential, *Nat. Commun.* 9 (2018) 1795.
- [41] M. Ma, X. Han, H.Q. Li, X.B. Zhang, Z.P. Zheng, L.Y. Zhou, J. Zheng, Z.X. Xie, Q. Kuang, L.S. Zheng, Tuning electronic structure of PdZn nanocatalyst via acid-etching strategy for highly selective and stable electrolytic nitrogen fixation under ambient conditions, *Appl. Catal. B Environ.* 265 (2020), 118568.
- [42] Y.C. Wan, H.J. Zhou, M.Y. Zheng, Z.H. Huang, F.Y. Kang, J. Li, R.T. Lv, Oxidation state modulation of bismuth for efficient electrocatalytic nitrogen reduction to ammonia, *Adv. Funct. Mater.* 31 (2021), 2100300.
- [43] Y. Ling, F.M.D. Kazim, S.X. Ma, Q. Zhang, K.G. Qu, Y.G. Wang, S.L. Xiao, W.W. Cai, Z.H. Yang, Strain induced rich planar defects in heterogeneous WS₂/WO₂ enable efficient nitrogen fixation at low overpotential, *J. Mater. Chem. A* 8 (2020) 12996–13003.
- [44] J.X. Yao, D. Bao, Q. Zhang, M.M. Shi, Y. Wang, R. Gao, J.M. Yan, Q. Jiang, Tailoring oxygen vacancies of BiVO₄ toward highly efficient noble-metal-free electrocatalyst for artificial N₂ fixation under ambient conditions, *Small Methods* 3 (2018), 1800333.
- [45] H. Wang, S. Liu, H. Zhang, S. Yin, Y. Xu, X. Li, Z. Wang, L. Wang, Three-dimensional Pd-Ag-S porous nanospores for electrocatalytic nitrogen reduction to ammonia, *Nanoscale* 12 (2020) 13507–13512.
- [46] L.Q. Li, C. Tang, B.Q. Xia, H.Y. Jin, Y. Zheng, S.Z. Qiao, Two-dimensional mosaic bismuth nanosheets for highly selective ambient electrocatalytic nitrogen reduction, *ACS Catal.* 9 (2019) 2902–2908.
- [47] Z. Chen, J.X. Zhao, L.C. Yin, Z.F. Chen, B-terminated (111) polar surfaces of BP and BAs: promising metal-free electrocatalysts with large reaction regions for nitrogen fixation, *J. Mater. Chem. A* 7 (2019) 13284–13292.
- [48] W. Song, Z. Fu, L. Fu, C.Z. He, Conversion of dinitrogen to ammonia by FeB-embedded graphyne, *J. Electrochem. Soc.* 168 (2021), 066503.
- [49] W.C. Xu, G.L. Fan, J.L. Chen, J.H. Li, L. Zhang, S.L. Zhu, X.C. Su, F.Y. Cheng, J. Chen, Nanoporous palladium hydride for electrocatalytic N₂ reduction under ambient conditions, *Angew. Chem. Int. Ed.* 59 (2020) 3511–3516.
- [50] X.Q. Han, Z.L. Lang, F.Y. Zhang, H.L. Xu, Z.M. Su, Computational evaluation of FeMo heteroatom coeffect induced high electroreduction activity of N₂-to-NH₃, *Appl. Surf. Sci.* 579 (2022), 152214.
- [51] X.Y. Liang, X.X. Deng, C. Guo, C.M.L. Wu, Activity origin and design principles for atomic vanadium anchoring on phosphorene monolayer for nitrogen reduction reaction, *Nano Res.* 13 (2020) 2925–2932.
- [52] Y.C. Wan, Z.J. Wang, J. Li, R.T. Lv, Mo₂C-MoO₂ heterostructure quantum dots for enhanced electrocatalytic nitrogen reduction to ammonia, *ACS Nano* 16 (2022) 643–654.